nature climate change

Article

https://doi.org/10.1038/s41558-026-02660-7

Shifting hail hazard under global warming and effects on crop hail risk

Received: 27 March 2025

Accepted: 29 April 2026

Published online: 3 June 2026

Check for updates

Timothy H. Raupach [1,2,3,4] ✉, Raphael Portmann [5,6], Christian Siderius [7] & Steven C. Sherwood [2,3,4]

Hailstorms cause damage across the globe and endanger crops, but their changes in a warming climate are not well quantified. Here we apply three hail proxies to an ensemble of global model projections to show divergent changes in hail-prone condition frequency worldwide. Changes depend on whether the proxy allows instability increases to be offset by temperature or moisture increases. Uncertainty on hail projections remains high, especially in the tropics. In projections with 2 °C and 3 °C of mean global warming, ensemble-mean hail-prone conditions shifted polewards, with decreases in hail hazard in the mid-latitudes and increases in colder regions. Across 26 crop types with fixed exposure and vulnerability, hail risk was generally projected to increase for winter crops such as wheat and decrease for summer crops such as maize. Poleward shifts in hail hazard may attenuate yield increases from similar shifts in crop regions under climate change.

Hailstorms are a form of extreme weather that causes substantial damage to physical assets including crops. Hail and the storms that produce it are expected to be affected by anthropogenic global warming, yet regional studies using observations or projections show geographical inhomogeneities and there remains high uncertainty on the details of changes[1]. Globally, hail observations are scarce[1], meaning that global climatologies generally rely on satellite data[2] or examination of environmental conditions in reanalyses using hail proxies[3].

Because hailstorms are hard to observe and model owing to their small spatial size and relative rarity[1], climatological studies often use proxies that detect hail-prone conditions. Hail proxies rely on detecting the atmospheric 'ingredients' required for hail to form. Hailstones form by accretion of supercooled liquid water onto ice embryos suspended in the updraft of a thunderstorm, until they become too heavy to support, after which they fall while melting on their descent through warmer air[4]. Hailstorm ingredients are usually considered to include, at minimum, atmospheric instability to allow for a thunderstorm with strong updrafts that can support hail growth to form[5], and vertical wind shear (differences in horizontal wind by height) to 'organize' the storm[6] and influence hailstone trajectories[7,8]. Instability–shear hail proxies are common, but may overestimate hail in tropical regions where instability is often high and wind shear may better discriminate hailstorm environments[9]. Proxies also suffer from the 'initiation problem', in that storms rarely initiate even in storm-prone conditions[10].

Climate change is expected to affect the ingredients for hailstorms and thus the frequency and severity of hail[1]. A thermodynamic expectation is of three offsetting effects: first, increased instability due to a larger saturation deficit in a warmer atmosphere[11] leading to more storm initiation and stronger updrafts that could support larger hailstones; second, increased melting of hailstones due to a warmer troposphere[12], leading to a reduction (or elimination[13]) of surface hail frequency; and third, an overall decrease in vertical wind shear[6] that is often outweighed by changes in instability[14] and may not apply locally[15]. The broad thermodynamic expectation is of reduced surface hail frequency combined with increased severity when hail does reach the Earth's surface[1]. However, regional studies show large geographical heterogeneity in hail frequency trends, owing partly to offsetting effects and partly to changes in large-scale dynamics, meaning that ingredient changes are not spatially uniform, while hail severity is generally expected to increase[1]. Process uncertainties, such as those around the influence of changes in aerosol concentrations, also remain[1].

[1]Institute for Climate Risk and Response, UNSW Sydney, Sydney, New South Wales, Australia. [2]Climate Change Research Centre, UNSW Sydney, Sydney, New South Wales, Australia. [3]ARC Centre of Excellence for Climate Extremes, UNSW Sydney, Sydney, New South Wales, Australia. [4]ARC Centre of Excellence for 21st Century Weather, UNSW Sydney, Sydney, New South Wales, Australia. [5]Agroscope, Climate and Agriculture, Zurich, Switzerland. [6]Planval, Bern, Switzerland. [7]Uncharted Waters, Sydney, New South Wales, Australia. ✉e-mail: timothy.h.raupach@gmail.com

https://doi.org/10.1038/s41558-026-02660-7

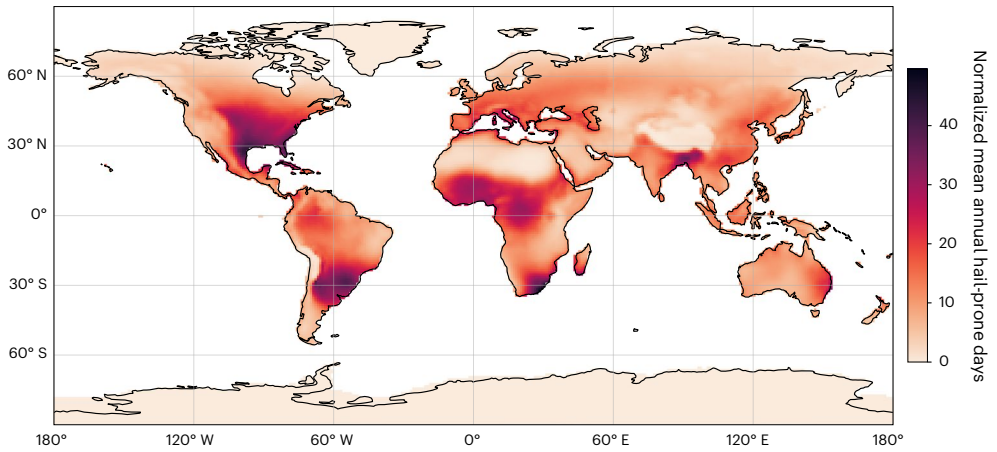

Fig. 1 | Multimodel, multiproxy mean normalized annual hail-prone days over the historical period. Hail proxies show known hail-prone regions that broadly agree with published climatologies. Multimodel, multiproxy mean (20 years, 3 proxies, 8 CMIP6 models and ERA5, $n = 540$ samples per grid point) of normalized annual hail-prone days for CMIP6 models and ERA5 reanalysis for 3 selected proxies over the historical period (1980–1999) at 1 × 1° resolution. Basemap data from Natural Earth (https://www.naturalearthdata.com).

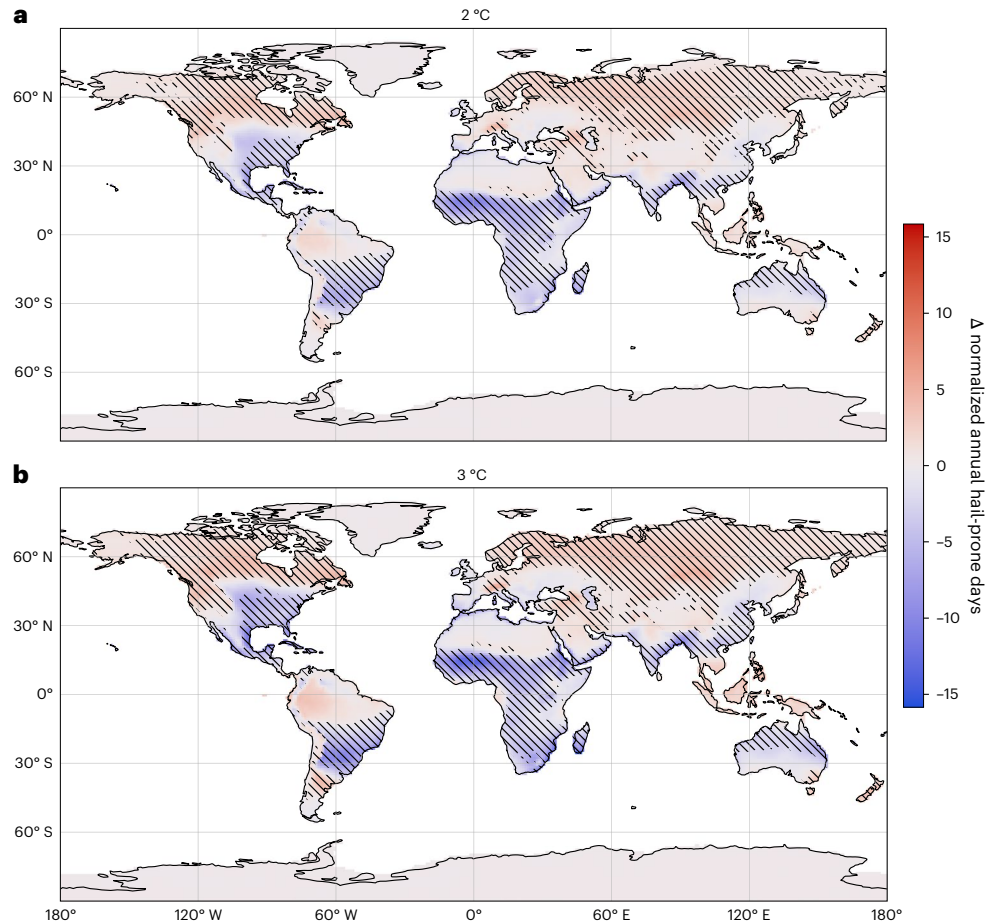

Fig. 2 | Changes in multiproxy, multimodel mean annual hail-prone days by future epoch. Hail-prone conditions shift under warming projections. **a**,**b**, Changes in multiproxy, multimodel mean normalized annual hail-prone days ($n = 480$ per grid point) for 2 °C (**a**) and 3 °C (**b**) of global warming. Stippling shows regions in which at least 50% of the model/proxy combinations agreed with the sign of the mean difference and also showed significant differences in the mean ($P < 0.05$ using a two-sided Welch's t-test, $n = 20$ years per epoch). Basemap data from Natural Earth (https://www.naturalearthdata.com).

Hailstorms can damage crops by wounding plants and increasing pathogen infection[16], breaking stems, defoliating or crushing plants[17], resulting in substantial yield losses[17]. Factors that affect crop damage inflicted by hail include the hailstone size[18] and number of hailstones per area[19], coincident horizontal wind[20] and crop growth stage[17,19,21]. Correlations between temperature and hailstorm damage in Europe[22] have been used to project regional increases in damage with warming[23], and in Switzerland, an increase in hail days has increased hail risk to winter

https://doi.org/10.1038/s41558-026-02660-7

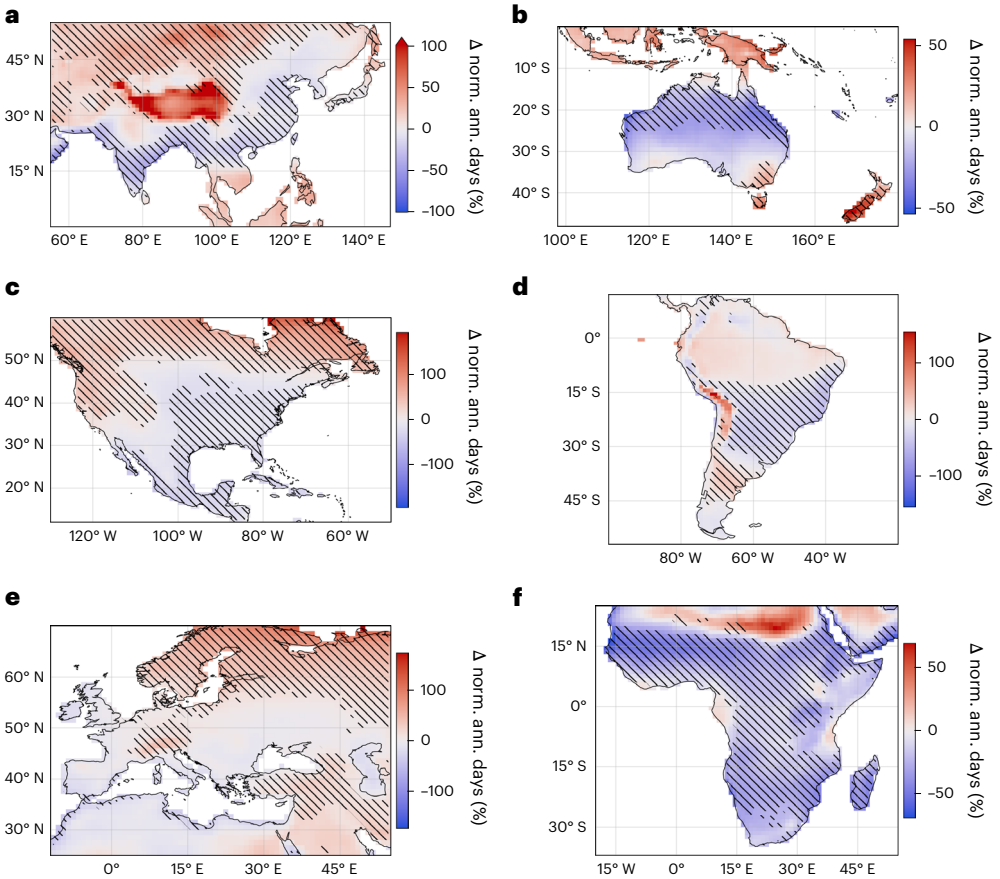

Fig. 3 | Relative changes in multiproxy, multimodel mean annual hail-prone days by region. a–f, Changes are shown as a percentage of multiproxy, multimodel mean normalized historical hail-prone days (norm. ann. days) ($n = 480$ per grid point) over land, for 3 °C warming, for Asia (**a**), Oceania (**b**), North America (**c**), South America (**d**), Europe (**e**) and Africa (**f**). Region 'shorthand' definitions are shown in Supplementary Section 1.1. Stippling as for Fig. 2. Colour bars are shared across rows, and the colour bar for **a** is truncated to increase contrast. Basemap data from Natural Earth (https://www.naturalearthdata.com).

wheat despite the harvesting date becoming earlier as temperatures increase[24]. However, no global picture on possible climate-induced changes to hail risk for crops has emerged.

Here, we applied three globally realistic hail proxies—the Raupach, Eccel and significant hail parameter (SHIP) proxies—to an ensemble of eight global projections from the Coupled Model Intercomparison Project Phase 6 (CMIP6)[25], to examine projections of the frequency of hail-prone conditions globally. We used a per-degree framework[26] for simpler comparisons between models. For details of the simulations and proxies used, refer to Methods and Supplementary Information. To validate the global proxy climatology, we compared the multimodel, multiproxy ensemble climatology with published local climatologies. We examined relative changes in hail-prone conditions between historical and warmer periods, overall and seasonally, and identified the primary drivers of changes. As a sensitivity study, we investigated the effects of projected changes on hail-prone proportions of time-invariant crop growing seasons for 26 different crops. Generally, hailstorm frequency is projected to shift polewards, with decreases in warmer environments and increases in cooler environments in future, driven primarily by increases in convective instability and offset by temperature or moisture increases. Our sensitivity analysis shows that the projected changes would generally increase hail occurrence risk for winter crops while decreasing the risk for summer crops.

Climatology and proxy validation

The multimodel, multiproxy climatology of normalized annual hail-prone days for 1980–1999 highlights known hail-prone regions globally (Fig. 1). While individual CMIP6 models produced a wide range of absolute values of hail-prone days, the locations of hail hotspots agreed well between reanalysis and models (Extended Data Fig. 1). Different proxies highlighted similar geographical regions but differed in magnitudes of hail-prone days, with the SHIP[27] producing the fewest, and the Eccel proxy[28] producing the greatest number of hail-prone days. Given the broad geographical agreement but differences in absolute numbers of hail-prone days, we use annual hail-prone days normalized by per-proxy per-model maxima, and focus primarily on changes in multiproxy, multimodel mean annual normalized hail-prone days in our analyses.

The Raupach, Eccel and SHIP proxies were trained in Australia[9], Italy[28] and the USA[27], respectively; therefore, to validate their global applicability, we performed a detailed comparison between the ensemble proxy results and published climatologies worldwide (Supplementary Section 1 and Supplementary Figs. 1–6). The Raupach proxy was designed to adapt to latitudinal changes in hail environments and was trained in Australia using data from the tropics to mid-latitudes, covering most environments in which hail is expected[9]. Generally, spatial agreement of the proxy ensemble with published climatologies was strong. The proxy ensemble disagreed with station reports (but not satellite or proxy studies) over the Tibetan Plateau, and in the USA some ensemble members placed the peak hail risk on the Gulf Coast rather than on the Great Plains. The proxy ensemble showed greater intermodel and interproxy disagreement over the tropics than over the mid-latitudes. Multiproxy means were able to identify particularly hail-prone periods in case studies from areas where the proxies were not trained (Supplementary Section 2, and Supplementary Figs. 7 and 8).

https://doi.org/10.1038/s41558-026-02660-7

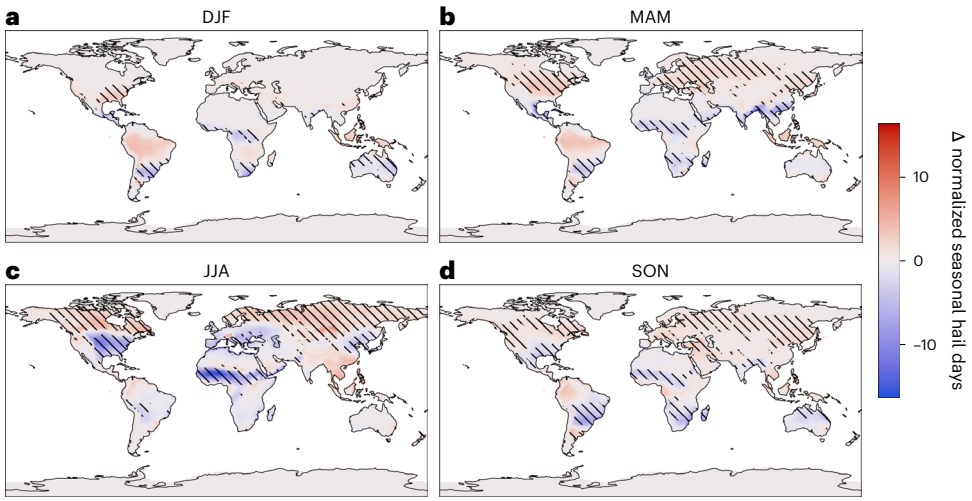

Fig. 4 | Changes in multimodel, multiproxy mean seasonal hail-prone days for 3 °C global warming. a–d, Seasons are December, January, February (DJF, **a**); March, April, May (MAM, **b**); June, July, August (JJA, **c**); and September, October, November (SON, **d**). Stippling as for Fig. 2. *n* = 480 per grid point. Basemap data from Natural Earth (https://www.naturalearthdata.com).

Changes in hail-prone days with warming

Changes in multimodel, multiproxy mean normalized annual hail-prone days for 2 °C and 3 °C of global warming show an overall poleward shift in hail-prone conditions under both warming scenarios (Fig. 2). Changes for 3 °C warming were similar to, but stronger than, those for 2 °C. Changes often agreed in sign across the Raupach proxy and SHIP, while the pure instability–shear proxy of Eccel[28] produced contrasting increases leading to proxy disagreement in the tropics (Extended Data Fig. 2). Increases in the frequency of hail-prone conditions were projected across land areas in central-northern Asia, New Zealand, southeastern Australia, North America north of about 50° N and in the northwestern USA, South America in the southern Pampas and westward to the Andes, and Europe north of about 60° N, in the vicinity of the Alps, and southeast of the Black Sea (Fig. 3). Decreases in hail-prone day frequency were projected in southeast coastal areas of India and China (connecting in a band across mainland Southeast Asia), northern Australia, southeast USA and Mexico, southeast South America east of the Andes between about 15° S and 30° S, and most of Africa south of 15° N (Fig. 3). Some mid-latitude overall decreases in hail-prone conditions consisted of warm-season decreases offset by smaller increases in the cool season, for example in the southeastern USA (Fig. 4).

Drivers of the projected changes

Projections showed increased extreme convective available potential energy (CAPE), wide decreases in extreme wind shear, and increases in mean temperature at 500 hPa and most-unstable-parcel mixing ratio (Supplementary Section 3 and Supplementary Figs. 9–11). The main drivers of projected changes in this study, measured as the difference between projected changes and changes when the future values for single ingredients were debiased, depended on the proxy (Fig. 5). Overall, increases in hail-prone environment frequency were driven by instability increases, while reductions in hail-prone environment frequency were driven by temperature-related or moisture-related (for SHIP) ingredients. The sums of changes across debiased ingredients were close to the projected changes where no ingredients were debiased, indicating that these results explain most of the projected changes, with the small differences that remain probably related to interactions between ingredients. The large differences between the Eccel proxy and the other proxies were caused by the instability–shear proxy reacting to increases in instability without explicitly accounting for offsetting due to temperature or moisture changes. Changes in SHIP were driven mainly by changes in the most unstable parcel mixing ratio, whereas in the Raupach proxy, increases in hail-prone days due to instability increases were offset by changes in melting-level height and temperature at 500 hPa.

Changes in hail-prone cropping periods

Projected proportions of crop growing time considered hail-prone, for 26 crops by world region, showed broad reductions in Africa and broad increases in Asia (Fig. 6). We used a new metric, the hail-prone proportion of the cropping season (HPP), defined as the proportion of total cropping days considered hail prone at a given location, in a given year and for a given crop, based on monthly irrigated and rain-fed cropped areas[29], to measure relative hail occurrence hazard per crop. For the historical period, the six crops with the highest hail hazard were sorghum, millet, groundnuts/peanuts, rice, soybeans and maize, with high hazard in the African tropics and southeast Africa, southeast North America and southeast South America (Extended Data Fig. 3). Warming was projected to reduce HPP for these crops in these regions while increasing HPP for crops grown in more poleward regions (Supplementary Fig. 13).

In Africa, all crops were projected to experience fewer hail-prone days, with regional increases not statistically significant (Extended Data Fig. 4). In Asia (Extended Data Fig. 5), responses varied, with decreasing hail hazard in India and southeastern China, but increases in HPP across the north leading to overall increases in hazard for many crops. Maize was projected to experience greater hazard in southeastern China but lesser hazard in the northeast, while HPP for wheat and rapeseed/canola increased in northeastern China. In Europe and Western Asia, most significant changes were increases, concentrated in a zonal band at around 60 °N and in regions around the European Alps, an area to the southeast of the Black Sea, and in southern Iran (Extended Data Fig. 6). Increases in HPP for rye were especially strong in Finland, Estonia, Latvia and the adjoining areas of Russia. In North America, there were significant increases for barley and rye, which showed regional increases in HPP across central and eastern USA, and Canada (Extended Data Fig. 7). For other crops, there were generally decreases in HPP projected in the southeast, with increases projected in the northwest and across northern Canada. In Oceania, barley was projected to have increased hail hazard, albeit with a large range in projected changes, while HPP decreased

https://doi.org/10.1038/s41558-026-02660-7

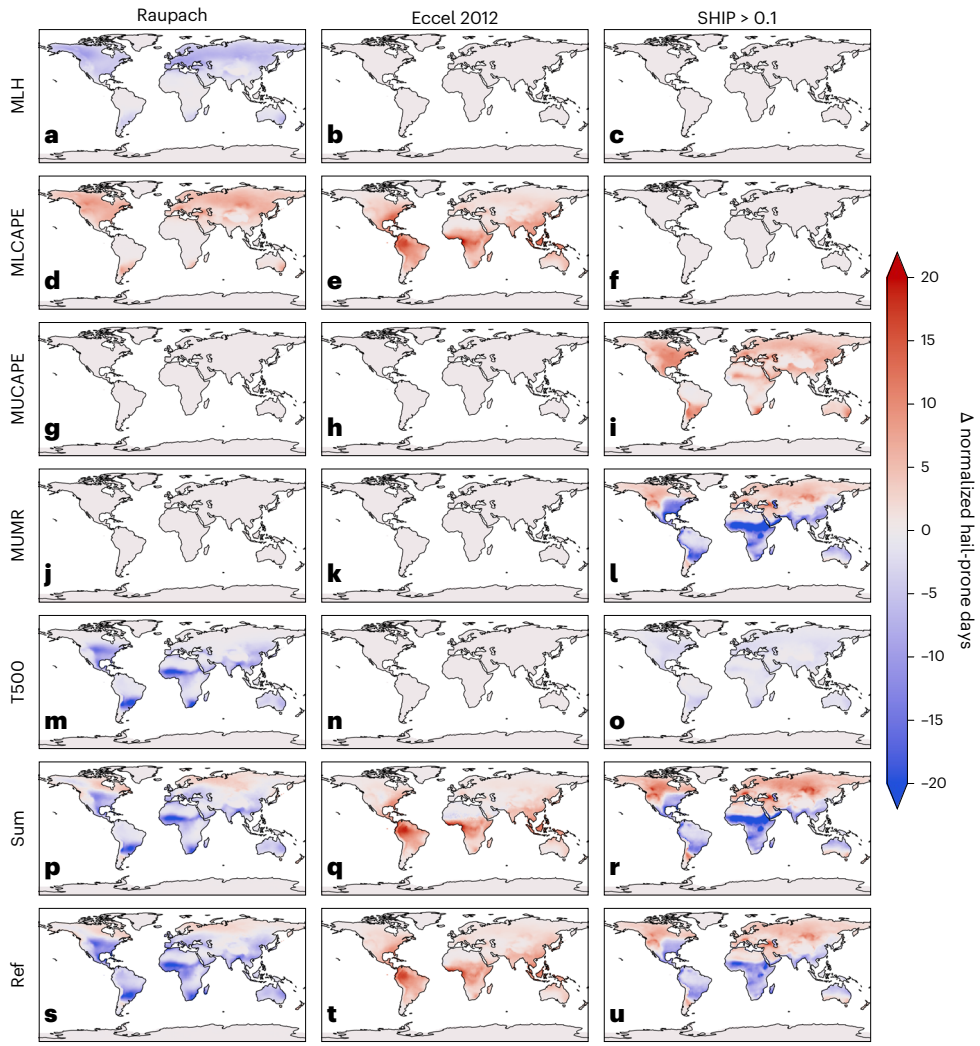

Fig. 5 | The main drivers of the projected changes. a–u, All plots are multimodel means. Plots show the difference in mean normalized annual hail-prone days (n = 160 per grid point) between historical and the 3 °C epoch for unchanged ingredients, minus the difference with the given ingredient debiased in the 3 °C epoch. Red (blue) areas show where an ingredient added to (subtracted from) the projected change. Ingredients shown here are melting level height (MLH, **a–c**), mixed-layer CAPE (MLCAPE, calculated using a well-mixed parcel on the lowest 100 hPa, **d–f**), most-unstable CAPE (MUCAPE, calculated using the parcel with the largest equivalent potential temperature over the lowest 250 hPa, **g–i**), most-unstable-parcel mixing ratio (MUMR, **j–l**) and temperature at 500 hPa (T500, **m–o**). 'Sum' (**p–r**) shows sums across changes from all debiased ingredients (column sums from Supplementary Fig. 12), and 'Ref' (**s–u**) shows the projected changes per proxy when no ingredients were debiased. Columns show hail proxies, and the colour scale is in normalized annual hail days. All proxy ingredients are shown in Supplementary Fig. 12. Basemap data from Natural Earth (https://www.naturalearthdata.com).

for all other crops. Significant decreases in HPP were concentrated in Australia's northeast, while significant increases were in a small region of southeast Australia and the South Island of New Zealand (Extended Data Fig. 8). In South America, all crops were projected to have decreased overall hazard, except date palm and sugar beet, which had few significant changes (Extended Data Table 1). However, regional changes show statistically significant increases in HPP for several crops in a region of the southern Pampas and west to the Andes (Extended Data Fig. 9).

Localized monthly changes (Supplementary Figs. 14–20) highlight that the crops with the greatest projected increases in risk were those with winter cropping periods, while those with the greatest reductions in risk were those that grow across summer. For example, in China, potatoes crop from May to September and were projected to have decreased risk, while wheat grows from October to April and was projected to have increased risk (Supplementary Fig. 15). Uncertainty was higher for summer months, with greater intermodel spread and with the sign of the change disagreeing between proxies for some months.

Discussion

We applied three hail proxies to eight global projections. Results were divergent: the Raupach and SHIP proxies, which explicitly include offsetting low-mid tropospheric temperature and moisture levels, respectively, projected decreases in hail-prone condition frequency across the tropics, while the instability–shear proxy of Eccel projected strong increases in these regions due to instability increases. This inconsistency may be explained by offsetting of instability increases in the tropics: the Raupach proxy, in particular, has a feature interaction where the melting-level height affects the relative importance of instability versus shear to the proxy[9] (Supplementary Section 6.1), and thus is less sensitive to increased instability in the tropics. Driver analysis shows this interaction, with the Raupach proxy less sensitive to instability in the tropics than in the mid-latitudes (Fig. 5d). Instability–shear proxies have a tendency to overestimate hail probability in the tropics[9], which motivated development of the Raupach proxy. The disagreement between proxy projections means there remains high uncertainty on projections on hail hazard changes, particularly in the tropics.

https://doi.org/10.1038/s41558-026-02660-7

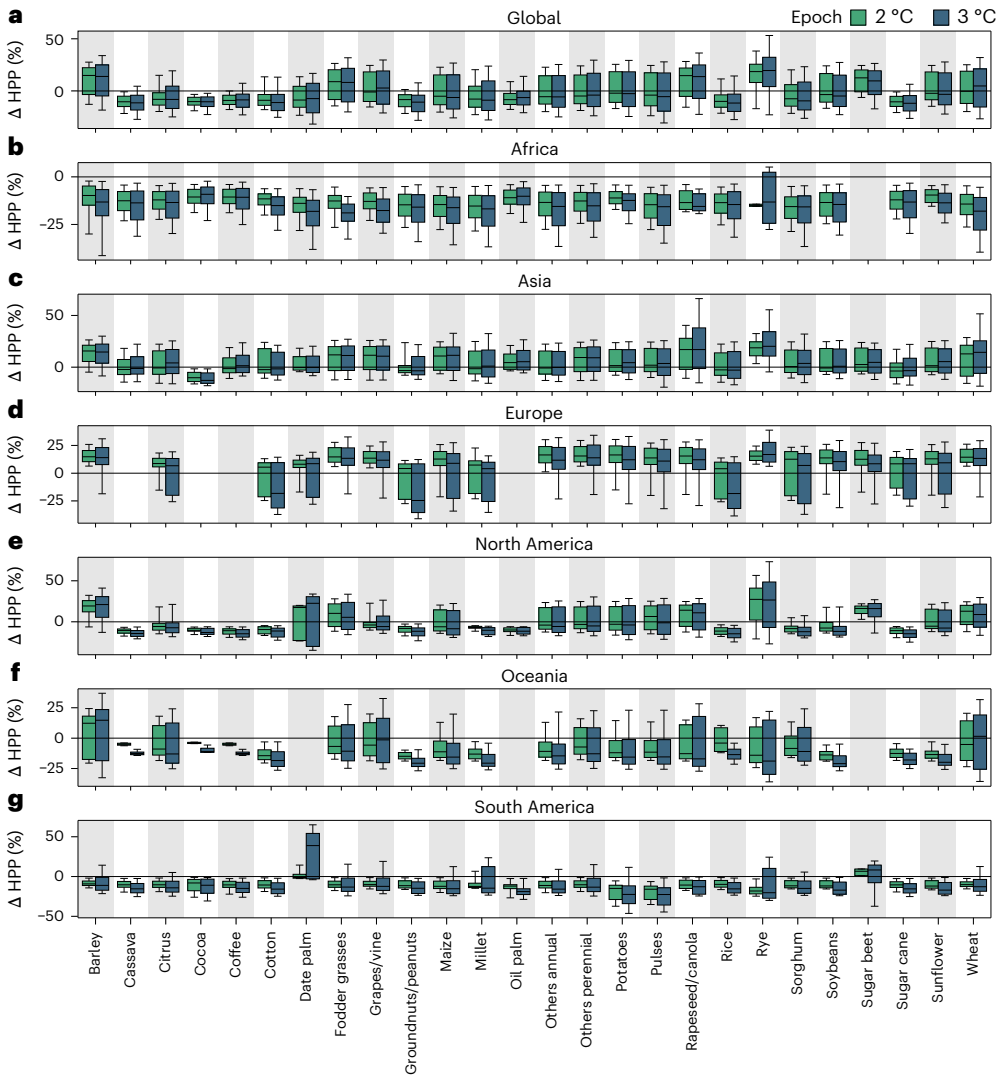

Fig. 6 | Distributions of significant changes in HPP by crop, epoch and world region. a–**g**, Changes are shown for Africa (**a**), Asia (**b**), Europe (**c**), North America (**e**), Oceania (**f**) and South America (**g**), as well as globally (**d**). Regions are defined as in Fig. 3. Changes are multimodel, multiproxy mean changes in HPP, shown as a percentage of the multimodel, multiproxy mean historical HPP. Significant changes are those for which at least 50% of the model/proxy combinations agreed with the sign of the mean difference and also showed significant differences in the mean ($P < 0.05$ using a two-sided Welch's t-test, $n = 20$ years per epoch). Horizontal bars show medians, coloured boxes show interquartile ranges and whiskers show 10th–90th percentile ranges. The numbers of samples in each box plot are provided in Extended Data Table 1.

We project broad poleward shifts in ensemble-mean hail-prone condition occurrence frequency under 2 °C and 3 °C of warming, with decreases in summer hail-prone day frequency and smaller increases in winter in some mid-latitude regions including the USA, Europe and Australia. The increases were driven by changes in instability and offset by increases in low-mid tropospheric temperature and moisture content. A sensitivity analysis showed that winter crops were most likely to have increased hail hazard while summer crops were most likely to experience reductions in hazard. We note that changes in crop risk depend heavily on crop vulnerability which changes during growing seasons[17]. Similar to the differences between the Eccel and Raupach/SHIP proxies, our results indicate that temperature-related effects such as melting of hail[13] mean that changes in hail-prone condition frequency may differ from those for all convective storms (regardless of whether they produce hail), which are generally projected to increase with warming[26]. We compare our results to previous studies in Supplementary Section 4.

We used CMIP6 projections that include changes in atmospheric circulations, thus avoiding a purely thermodynamic approach. Our projections align with projections of poleward shifts in storm tracks[30,31] and the observed expansion of the tropics[32]. However, we note that there is generally low confidence in how changes in dynamics affect extreme events[33], and for the broader class of severe convective storms (irrespective of hail occurrence), changes in reanalysis periods[34] can be of different sign to projected changes[26], which may be partly explained by uncertainty introduced by changes in atmospheric circulation. Future work should consider quantification of the relative importance of dynamic versus thermodynamic changes on hail frequency globally. Proxies trained in one region cannot be assumed to be perfectly applicable globally because storm properties differ by location[5,9]. However, the Raupach proxy is designed to take spatial variability in storm conditions into account and performs reasonably across the Australian continent, which contains a wide variety of storm environments[35], and we validated the ensemble-mean proxy results against published climatologies (Supplementary Section 1). The assumption of proxy stationarity in future climates introduces uncertainty and should be tested. We did not consider ocean areas because the proxies here were trained over land[9,28], maritime hailstorms may exhibit characteristics

distinct from land storms[36], and there remains uncertainty in the occurrence of hail in maritime storms[4].

Our results contribute to understanding climate impacts on global food production. Most previous studies have concentrated on temperature, precipitation and CO_2 changes, and neglect infrequent but high-impact extreme weather[37]. A limitation to our approach is our use of stationary and relatively coarse crop data, so our analysis of crop changes form a sensitivity study rather than projections for crop damage or yield. Suitable growing regions and cropping periods may also shift polewards with warming[38], with some positive impacts on yields[37]. Similar shifts in hail hazard may attenuate any positive impact on crop yields in a warming world. For maize, an important staple crop grown in tropical regions, a potential reduction in hail hazard would only lessen the projected severe reductions in yield driven by increasing temperatures[37]. Importantly, crop damage from hail depends on numerous factors including hailstone sizes and coincident wind strength[20]. Also, the timing of hail events within the broad cropping season strongly influences possible crop damage, because crop vulnerability to hail depends on the growth stage[17]. Future analyses should take projected changes in cropping season[24] and growth stages into account.

We show projected changes in hail-prone day frequency, with proxy limitations precluding examination of changes in hailstorm severity or hailstone size. Increases in atmospheric instability (Supplementary Fig. 9) in regions with sufficient moisture availability would generally be expected to increase generation of large hailstones that could survive melting[1], so severity may increase while frequency decreases. However, it remains difficult to draw conclusions on hail size from environmental proxies, given complicated offsetting and seasonally dependent effects of ingredient changes[39]. A coincident decrease of small hail and increase of large hail aligns has been projected for the end of the century in the USA[40], pseudo-global-warming simulations in the USA have shown a seasonal shift with increasing hailstone sizes in cold-season storms[39], and end-of-century increases in hailstone size are projected for some cities in Australia[41]. While it is likely that global severe hail projections would differ from the 'any hail' projections shown here, the possibility of some areas experiencing compounding risks with increased hail frequency in the cold season combined with increased hailstone size[39,42] may produce a pronounced risk to winter crops that merits further investigation.

Online content

Any methods, additional references, Nature Portfolio reporting summaries, source data, extended data, supplementary information, acknowledgements, peer review information; details of author contributions and competing interests; and statements of data and code availability are available at https://doi.org/10.1038/s41558-026-02660-7.

References

1. Raupach, T. H. et al. The effects of climate change on hailstorms. *Nat. Rev. Earth Environ.* **2**, 213–226 (2021).
2. Bang, S. D. & Cecil, D. J. Constructing a multifrequency passive microwave hail retrieval and climatology in the GPM domain. *J. Appl. Meteorol.* **58**, 1889–1904 (2019).
3. Prein, A. F. & Holland, G. J. Global estimates of damaging hail hazard. *Weather Clim. Extrem.* **22**, 10–23 (2018).
4. Knight, C. A. & Knight, N. C. in *Severe Convective Storms* (ed. Doswell, C. A.) 223–254 (American Meteorological Society, 2001).
5. Brooks, H. E., Lee, J. W. & Craven, J. P. The spatial distribution of severe thunderstorm and tornado environments from global reanalysis data. *Atmos. Res.* **67-68**, 73–94 (2003).
6. Brooks, H. E. Severe thunderstorms and climate change. *Atmos. Res.* **123**, 129–138 (2013).
7. Lin, Y. & Kumjian, M. R. Influences of CAPE on hail production in simulated supercell storms. *J. Atmos. Sci.* **79**, 179–204 (2022).
8. Fischer, J., Kunz, M., Lombardo, K. & Kumjian, M. R. Hail trajectories in a wide spectrum of supercell-like updrafts. *J. Atmos. Sci.* **82**, 1403–1422 (2025).
9. Raupach, T. H., Soderholm, J., Protat, A. & Sherwood, S. C. An improved instability-shear hail proxy for Australia. *Mon. Weather Rev.* **151**, 545–567 (2023).
10. Tippett, M. K., Allen, J. T., Gensini, V. A. & Brooks, H. E. Climate and hazardous convective weather. *Curr. Clim. Change Rep.* **1**, 60–73 (2015).
11. Seeley, J. T. & Romps, D. M. Why does tropical convective available potential energy (CAPE) increase with warming? *Geophys. Res. Lett.* **42**, 10,429–10,437 (2015).
12. Prein, A. F. & Heymsfield, A. J. Increased melting level height impacts surface precipitation phase and intensity. *Nat. Clim. Change* **10**, 771–776 (2020).
13. Mahoney, K., Alexander, M. A., Thompson, G., Barsugli, J. J. & Scott, J. D. Changes in hail and flood risk in high-resolution simulations over Colorado's mountains. *Nat. Clim. Change* **2**, 125–131 (2012).
14. Trapp, R. J., Diffenbaugh, N. S. & Gluhovsky, A. Transient response of severe thunderstorm forcing to elevated greenhouse gas concentrations. *Geophys. Res. Lett.* **36**, L01703 (2009).
15. Rädler, A. T., Groenemeijer, P. H., Faust, E., Sausen, R. & Púčik, T. Frequency of severe thunderstorms across Europe expected to increase in the 21st century due to rising instability. *npj Clim. Atmos. Sci.* **2**, 30 (2019).
16. Battaglia, M., Lee, C., Thomason, W., Fike, J. & Sadeghpour, A. Hail damage impacts on corn productivity: a review. *Crop Sci.* **59**, 1–14 (2019).
17. Dhillon, G. S. et al. Effects of simulated hail damage and foliar-applied recovery treatments on growth and grain yield of wheat, field pea, and dry bean crops. *Can. J. Plant Sci.* **101**, 758–769 (2021).
18. Changnon, S. A. Hailfall characteristics related to crop damage. *J. Appl. Meteorol.* **10**, 270–274 (1971).
19. Yue, Y., Zhou, L., Zhu, A.-x. & Ye, X. Vulnerability of cotton subjected to hail damage. *PLoS ONE* **14**, 1–21 (2019).
20. Morgan, G. M. & Towery, N. G. On the role of strong winds in damage to crops by hail and its estimation with a simple instrument. *J. Appl. Meteorol.* **15**, 891–898 (1976).
21. Sánchez, J. L. et al. Crop damage: the hail size factor. *J. Appl. Meteorol.* **35**, 1535–1541 (1996).
22. Dessens, J. Severe convective weather in the context of a nighttime global warming. *Geophys. Res. Lett.* **22**, 1241–1244 (1995).
23. Botzen, W. J. W., Bouwer, L. M. & Bergh, J. C. J. M. V. D. Climate change and hailstorm damage: empirical evidence and implications for agriculture and insurance. *Resour. Energy Econ.* **32**, 341–362 (2010).
24. Portmann, R. et al. Earlier harvest but more hail–hail risk to winter wheat in Switzerland since 1972. *Meteorol. Z.* **34**, 293–306 (2026).
25. Eyring, V. et al. Overview of the Coupled Model Intercomparison Project Phase 6 (CMIP6) experimental design and organization. *Geosci. Model Dev.* **9**, 1937–1958 (2016).
26. Lepore, C., Abernathey, R., Henderson, N., Allen, J. T. & Tippett, M. K. Future global convective environments in CMIP6 models. *Earths Future* **9**, e2021EF002277 (2021).
27. *Significant hail parameter* (National Oceanographic and Atmospheric Administration National Weather Service Storm Prediction Center, accessed 21 June 2022); https://www.spc.noaa.gov/exper/mesoanalysis/help/help_sigh.html
28. Eccel, E., Cau, P., Riemann-Campe, K. & Biasioli, F. Quantitative hail monitoring in an Alpine area: 35-year climatology and links with atmospheric variables. *Int. J. Climatol.* **3**, 503–517 (2012).

29. Portmann, F. T., Siebert, S. & Döll, P. MIRCA2000—global monthly irrigated and rainfed crop areas around the year 2000: a new high-resolution data set for agricultural and hydrological modeling. *Glob. Biogeochem. Cycles* **24**, GB1011 (2010).
30. Yin, J. H. A consistent poleward shift of the storm tracks in simulations of 21st century climate. *Geophys. Res. Lett.* **32**, L18701 (2005).
31. Tamarin, T. & Kaspi, Y. The poleward shift of storm tracks under global warming: a Lagrangian perspective. *Geophys. Res. Lett.* **44**, 10,666–10,674 (2017).
32. Heffernan, O. The mystery of the expanding tropics. *Nature* **530**, 20–22 (2016).
33. Seneviratne, S. et al. in *Climate Change 2021: The Physical Science Basis. Contribution of Working Group I to the Sixth Assessment Report of the Intergovernmental Panel on Climate Change* (eds Masson-Delmotte, V. et al.) Section 11, 1513–1765 (Cambridge Univ. Press, 2021); https://www.ipcc.ch/report/ar6/wg1/downloads/report/IPCC_AR6_WGI_Chapter11.pdf
34. Taszarek, M., Allen, J. T., Marchio, M. & Brooks, H. E. Global climatology and trends in convective environments from ERA5 and rawinsonde data. *npj Clim. Atmos. Sci.* **4**, 35 (2021).
35. Raupach, T. H., Soderholm, J. S., Warren, R. A. & Sherwood, S. C. Changes in hail hazard across Australia: 1979–2021. *npj Clim. Atmos. Sci.* **6**, 143 (2023).
36. Sari, F. P. & Lasher-Trapp, S. Hailstorm events over a maritime tropical region: storm environments and characteristics. *J. Geophys. Res. Atmos.* **130**, e2024JD042718 (2025).
37. Jägermeyr, J. et al. Climate impacts on global agriculture emerge earlier in new generation of climate and crop models. *Nat. Food* **2**, 873–885 (2021).
38. Franke, J. A. et al. Agricultural breadbaskets shift poleward given adaptive farmer behavior under climate change. *Glob. Chang. Biol.* **28**, 167–181 (2022).
39. Mallinson, H., Lasher-Trapp, S., Trapp, J., Woods, M. & Orendorf, S. Hailfall in a possible future climate using a pseudo-global warming approach: hail characteristics and mesoscale influences. *J. Clim.* **37**, 527–549 (2024).
40. Gensini, V. A. et al. Hailstone size dichotomy in a warming climate. *npj Clim. Atmos. Sci.* **7**, 185 (2024).
41. Raupach, T. H. & Aldridge, J. Changes in hail damage potential in major Australian cities with global warming. *Geophys. Res. Lett.* **52**, e2025GL117676 (2025).
42. Battaglioli, F., Taszarek, M., Groenemeijer, P., Púčik, T. & Rädler, A. Contrasting trends in very large hail events and related economic losses across the globe. *Nat. Geosci.* **19**, 52–58 (2026).

Methods

Data

A filtering approach was used to select models from the CMIP6[25]. We selected models that contained variables required to calculate convective indices: air temperature at the surface (tas) and by model level (ta), wind vectors at the surface (uas and vas) and by level (ua and va), specific humidity at the surface (huss) and by level (hus), and surface pressure (ps). We filtered for models with a temporal resolution at least as fine as 6-hourly (those with 'table IDs' of 3hr or 6hrLev), and models that were available for both historical and SSP5-8.5 experiments ('experiment IDs' of historical or ssp585). Furthermore, the models had to be available in the National Computational Infrastructure node of the Earth System Grid Federation (ESGF) and had to cover the required epochs. The resulting CMIP6 models, that we used here[43–58], are detailed in Supplementary Table 1. Model data were used at 6-hourly temporal resolution. If model orography was available in the orog variable, it was used; if not, the orography of the historical runs of CNRM-CM6-1 (ensemble r1i1p1f2) was interpolated onto the model grid and used instead[59]. Reanalyses were based on European Centre for Medium-range Weather Forecasts (ECMWF) reanalysis 5 (ERA5) data[60] on pressure levels. To match the CMIP6 model characteristics, we used global ERA5 data at 00, 06, 12 and 18 UTC for each day from 1980 to 1999, interpolated to 1° × 1° resolution. Cropping periods for each 1° × 1° grid point were calculated as the union of all monthly cropping periods, per crop, from MIRCA2000[29] data at 0.5° × 0.5° resolution. MIRCA2000 provides global cropping months for 26 crops for the year 2000; we considered both rain-fed and irrigated crops. The cropping season is defined at a monthly timescale. If a month belongs to the cropping season of a particular crop at a particular location in MIRCA2000, all days of this month are considered cropping days. Crop vulnerability to hail depends strongly on the crop growth stage[17]. Here, we used the full cropping period including phases of low and high vulnerability.

Calculation of convective parameters

Convective parameters were calculated as described for the proxy of ref. 9, for each CMIP6 dataset at its native resolution and for downscaled ERA5 data. For each CMIP6 model, annual and seasonal statistics were calculated, and then all statistics were interpolated onto a 1° × 1° grid for comparison.

Application of hail proxies

We applied three hail-specific instability-shear proxies—Raupach, Eccel and SHIP—to CMIP6 and ERA5 data. The proxies were, respectively, the Raupach proxy, a modified version of the proxy in ref. 9, the Eccel proxy of ref. 28, and SHIP, a threshold of 0.1 on the SHIP[27]. The proxies are described in detail in Supplementary Section 6. Proxy results were masked to land areas, as the proxies were trained on land-based reports and no surface-based climatologies are available for ocean regions. Proxy outputs (binary hail prone or not hail prone) were collated into annual hail-prone days.

Proxy normalization

To give proxies equal weighting when calculating multimodel, multiproxy means, annual hail-prone days were normalized per model and proxy. The three proxies produced binary outputs, classifying each day as hail prone or not hail prone. Annual hail-prone days were the sum of all hail-prone days per year per location. To account for differences between the proxies and between models, and to allow each proxy to have the same weight when calculating multimodel, multiproxy means, annual hail-prone days (AHPD) were normalized per proxy and per model, such that

$$\mathrm{AHPD}_{m,p,i,j,y} = \frac{\mathrm{AHPD}_{m,p,i,j,y}}{\max([\mathrm{AHPD}_{m,p,i,j,y}\ \forall\, i,j,y])} \times 100, \quad (1)$$

where m, p, i, j and y are indices for model, proxy, longitude, latitude and year, respectively.

Per-degree framework

The historical period used for each model was 1980–1999. The epochs that represented 2 °C and 3 °C warming compared with the historical period were determined per model using 20-year running means of monthly global average temperature anomalies (Supplementary Fig. 21).

Calculation of drivers

For each hail proxy ingredient, debiased versions of the 3 °C epoch were calculated using python-cmethods[61] using the quantile-mapping method with 100 quantiles and the historical period as the baseline. Annual hail-prone days in the debiased datasets were normalized by the same factor used in the non-debiased data.

Data availability

MIRCA2000 data are available via Zenodo at https://doi.org/10.5281/zenodo.7422506 (ref. 62). ERA5 data are available at https://www.ecmwf.int/en/forecasts/dataset/ecmwf-reanalysis-v5 (ref. 63). CMIP6 data are available at https://pcmdi.llnl.gov/CMIP6/ (refs. 43–58), with licences presented in Supplementary Table 2.

Code availability

Convective indices were calculated using xarray_parcel by T.H.R., available via Zenodo at https://doi.org/10.5281/zenodo.7073521 (ref. 64). Warming levels were calculated using code by T.H.R., available via Zenodo at https://doi.org/10.5281/zenodo.10785698 (ref. 65). Debiasing code was python-cmethods by B. T. Schwertfeger, available via Zenodo at https://doi.org/10.5281/zenodo.12168002 (ref. 61). All study code is available via Zenodo at https://doi.org/10.5281/zenodo.15099057 (ref. 66); this article used version v1.0.5 of the code.

References

43. Lovato, T. & Peano, D. CMCC CMCC-CM2-SR5 model output prepared for CMIP6 CMIP historical. *World Climate Research Programme* https://doi.org/10.22033/ESGF/CMIP6.3825 (2020).
44. Lovato, T. & Peano, D. CMCC CMCC-CM2-SR5 model output prepared for CMIP6 ScenarioMIP ssp585. *World Climate Research Programme* https://doi.org/10.22033/ESGF/CMIP6.3896 (2020).
45. Lovato, T., Peano, D. & Butenschön, M. CMCC CMCC-ESM2 model output prepared for CMIP6 CMIP historical. *World Climate Research Programme* https://doi.org/10.22033/ESGF/CMIP6.13195 (2021).
46. Lovato, T., Peano, D. & Butenschön, M. CMCC CMCC-ESM2 model output prepared for CMIP6 ScenarioMIP ssp585. *World Climate Research Programme* https://doi.org/10.22033/ESGF/CMIP6.13259 (2021).
47. Voldoire, A. CMIP6 simulations of the CNRM-CERFACS based on CNRM-CM6-1 model for CMIP experiment historical. *World Climate Research Programme* https://doi.org/10.22033/ESGF/CMIP6.4066 (2018).
48. Voldoire, A. CNRM-CERFACS CNRM-CM6-1 model output prepared for CMIP6 ScenarioMIP ssp585. *World Climate Research Programme* https://doi.org/10.22033/ESGF/CMIP6.4224 (2019).
49. EC-Earth Consortium (EC-Earth). EC-Earth-Consortium EC-Earth3 model output prepared for CMIP6 CMIP historical. *World Climate Research Programme* https://doi.org/10.22033/ESGF/CMIP6.4700 (2019).
50. EC-Earth Consortium (EC-Earth). EC-Earth-Consortium EC-Earth3 model output prepared for CMIP6 ScenarioMIP ssp585. *World Climate Research Programme* https://doi.org/10.22033/ESGF/CMIP6.4912 (2019).

51. NASA Goddard Institute for Space Studies (NASA/GISS). NASA-GISS GISS-E2.1G model output prepared for CMIP6 CMIP historical. *World Climate Research Programme* https://doi.org/10.22033/ESGF/CMIP6.7127 (2018).
52. NASA Goddard Institute for Space Studies (NASA/GISS). NASA-GISS GISS-E2.1G model output prepared for CMIP6 ScenarioMIP ssp585. *World Climate Research Programme* https://doi.org/10.22033/ESGF/CMIP6.7460 (2020).
53. Tatebe, H. & Watanabe, M. MIROC MIROC6 model output prepared for CMIP6 CMIP historical. *World Climate Research Programme* https://doi.org/10.22033/ESGF/CMIP6.5603 (2018).
54. Shiogama, H., Abe, M. & Tatebe, H. MIROC MIROC6 model output prepared for CMIP6 ScenarioMIP ssp585. *World Climate Research Programme* https://doi.org/10.22033/ESGF/CMIP6.5771 (2019).
55. Jungclaus, J. et al. MPI-M MPI-ESM1.2-HR model output prepared for CMIP6 CMIP historical. *World Climate Research Programme* https://doi.org/10.22033/ESGF/CMIP6.6594 (2019).
56. Schupfner, M. et al. DKRZ MPI-ESM1.2-HR model output prepared for CMIP6 ScenarioMIP ssp585. *World Climate Research Programme* https://doi.org/10.22033/ESGF/CMIP6.4403 (2019).
57. Yukimoto, S. et al. MRI MRI-ESM2.0 model output prepared for CMIP6 CMIP historical. *World Climate Research Programme* https://doi.org/10.22033/ESGF/CMIP6.6842 (2019).
58. Yukimoto, S. et al. MRI MRI-ESM2.0 model output prepared for CMIP6 ScenarioMIP ssp585. *World Climate Research Programme* https://doi.org/10.22033/ESGF/CMIP6.6929 (2019).
59. Bracegirdle, T. J. et al. Twenty first century changes in Antarctic and Southern Ocean surface climate in CMIP6. *Atmos. Sci. Lett.* **21**, e984 (2020).
60. Hersbach, H. et al. The ERA5 global reanalysis. *Q. J. R. Meteorol. Soc.* **146**, 1999–2049 (2020).
61. Schwertfeger, B. T. btschwertfeger/python-cmethods: v2.3.0. *Zenodo* https://doi.org/10.5281/zenodo.12168002 (2024).
62. Portmann, F. T., Siebert, S. & Döll, P. Mirca2000. *Zenodo* https://doi.org/10.5281/zenodo.7422506 (2022).
63. Hersbach, H. et al. ERA5 hourly data on pressure levels from 1979 to present. *Copernicus Climate Change Service (C3S) Climate Data Store (CDS)* https://doi.org/10.24381/cds.bd0915c6 (2018).
64. Raupach, T. H. traupach/xarray_parcel: v1.0.5. *Zenodo* https://doi.org/10.5281/zenodo.7073521 (2025).
65. Raupach, T. H. Code to calculate warming levels from CMIP6 and CMIP5. *Zenodo* https://doi.org/10.5281/zenodo.10785698 (2024).
66. Raupach, T. traupach/future_hail_global: v1.0.5. *Zenodo* https://doi.org/10.5281/zenodo.15099057 (2026).

Acknowledgements

This research was supported by the Australian Government's National Collaborative Research Infrastructure Strategy (NCRIS), with computational resources provided by the National Computational Infrastructure (NCI) through the National Computational Merit Allocation Scheme and the UNSW HPC Scheme (DOI: 10.26190/PMN5-7J50). T.H.R. acknowledges financial support from QBE Insurance. R.P. acknowledges funding by the Swiss National Science Foundation (SNSF) Sinergia grant CRSII_201792.

Author contributions

T.H.R. designed the study, performed the analyses, wrote the paper and created the figures. R.P. suggested the crop analysis. R.P., C.S. and S.C.S. contributed to the design of analyses, interpretation of results and editing of the paper.

Funding

Open access funding provided through UNSW Library.

Competing interests

T.H.R.'s position at UNSW Sydney is financially supported by QBE Insurance. The other authors declare no competing interests.

Additional information

Extended data is available for this paper at https://doi.org/10.1038/s41558-026-02660-7.

Supplementary information The online version contains supplementary material available at https://doi.org/10.1038/s41558-026-02660-7.

Correspondence and requests for materials should be addressed to Timothy H. Raupach.

Peer review information *Nature Climate Change* thanks Susanna Mohr and the other, anonymous, reviewer(s) for their contribution to the peer review of this work.

https://doi.org/10.1038/s41558-026-02660-7

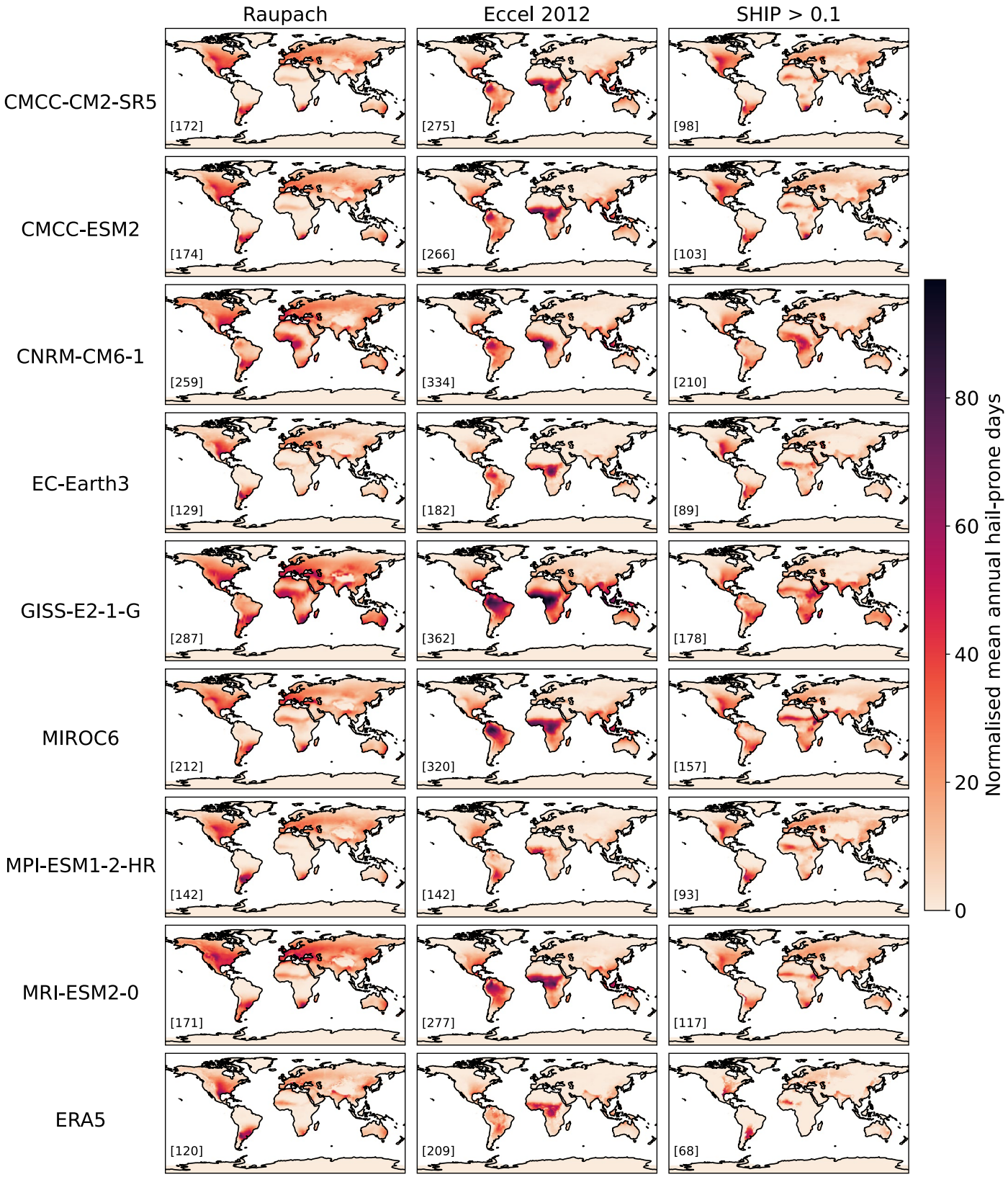

Extended Data Fig. 1 | Mean annual hail-prone days in historical (1980-1999) runs. n = 20 per grid point. There is one row per model (each CMIP6 model and ERA5 reanalysis), and one column per proxy. Inset numbers in square brackets show the normalisation factor by which each map was scaled, the maximum annual hail-prone days over the historical period. The models MPI-ESM1-2-HR and EC-Earth produced similar numbers of hail-prone days to ERA5, while MIROC6, CMCC-CM2-SR5, CMCC-ESM2, and MRI-ESM2-0 showed moderately more and CNRM-CM6-1 and GISS-E2-1-G showed considerably more hail-prone days than ERA5.

https://doi.org/10.1038/s41558-026-02660-7

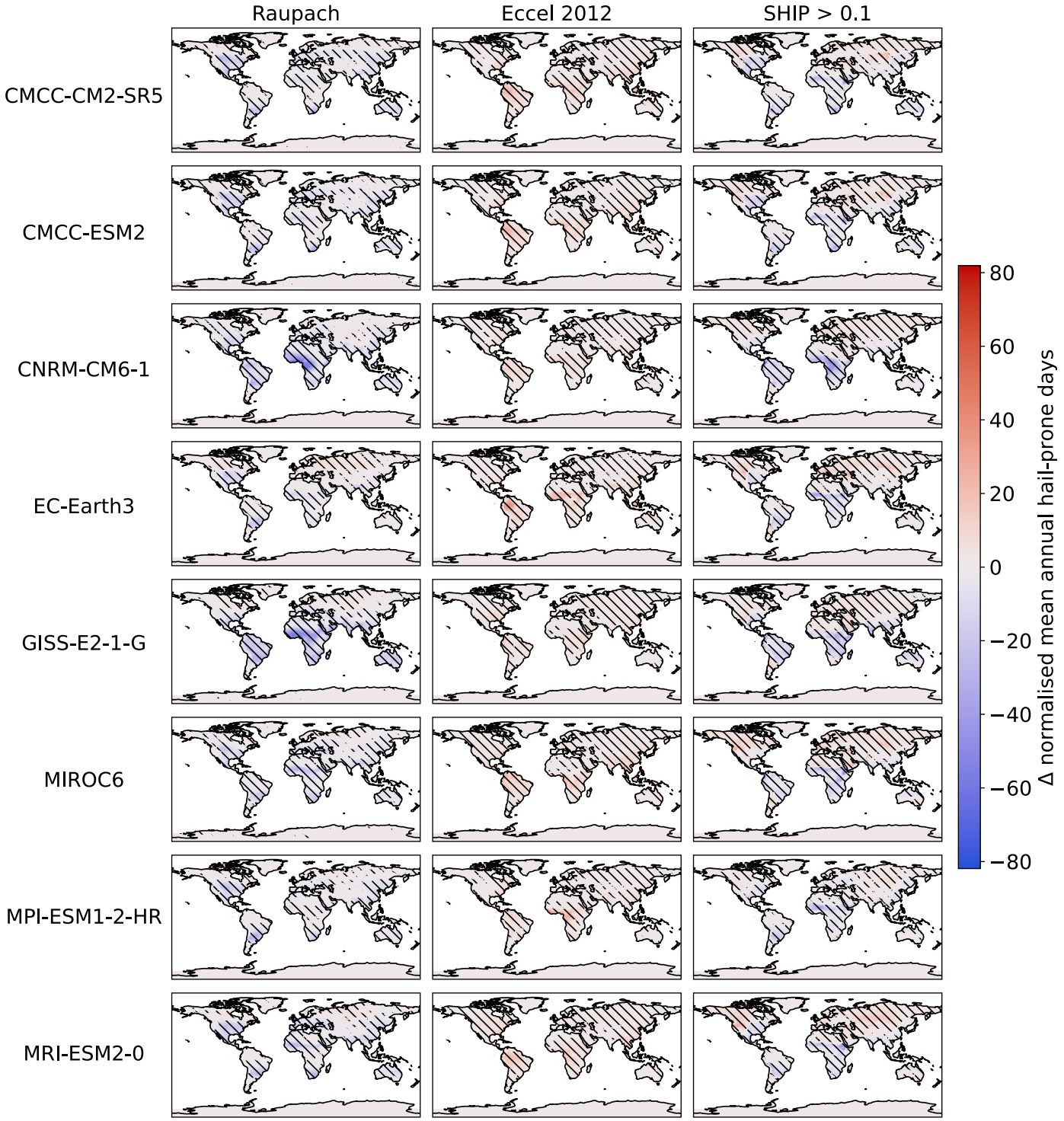

Extended Data Fig. 2 | Differences in mean annual hail-prone days by model and proxy for 3 °C global warming. Stippling shows regions for which the difference between epochs was statistically significant ($p < 0.05$ using a two-sided Welch's t-test, n = 20 years per epoch).

https://doi.org/10.1038/s41558-026-02660-7

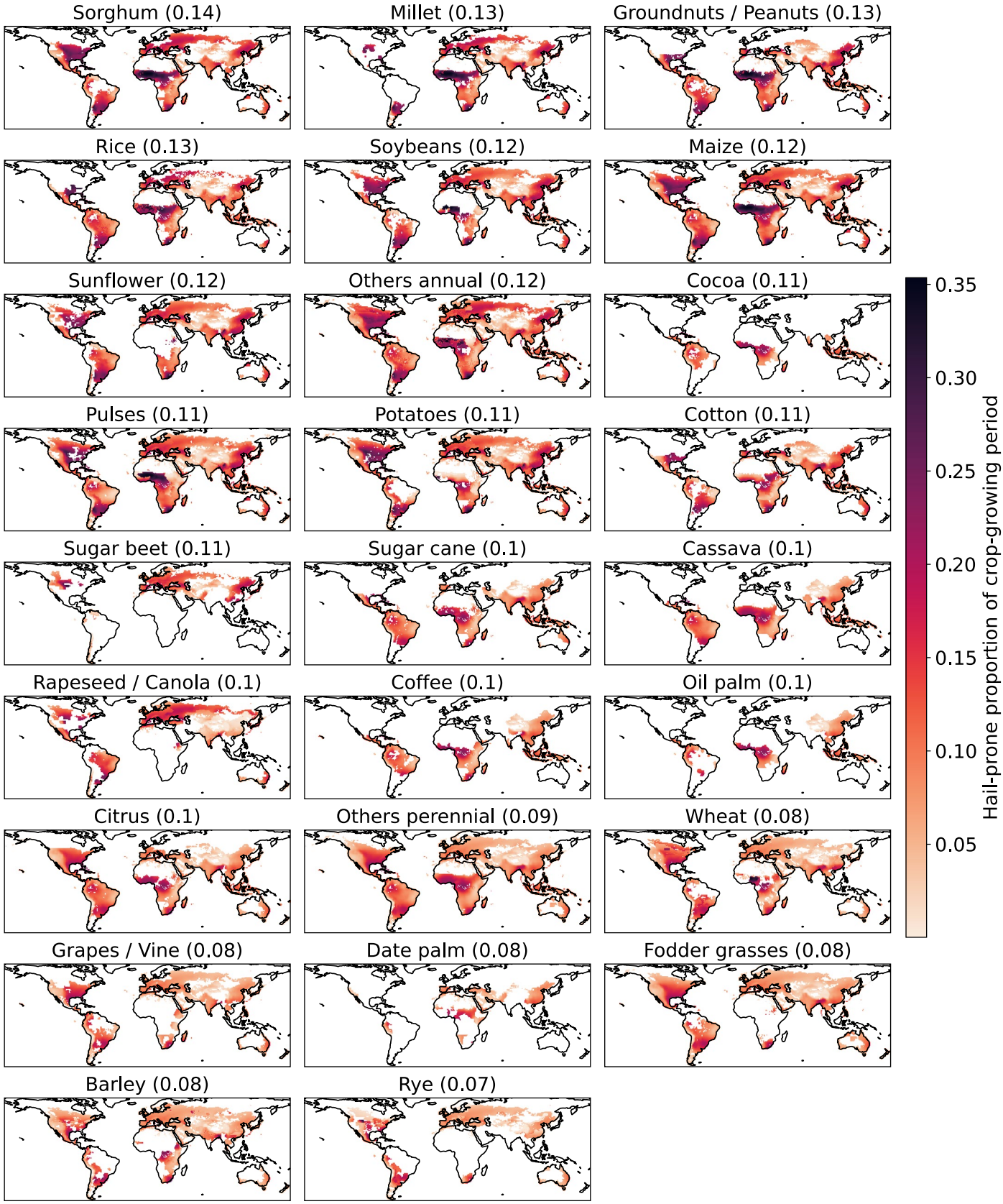

Extended Data Fig. 3 | Multimodel, multi-proxy mean hail-prone proportions of cropping seasons for the historical period. n = 480 per grid point. Brackets in titles show the spatial average of mean hail-prone proportion of cropping seasons by crop (numbers of samples shown in Supplementary Table 3). Plots are subset to remove areas with no crop data.

https://doi.org/10.1038/s41558-026-02660-7

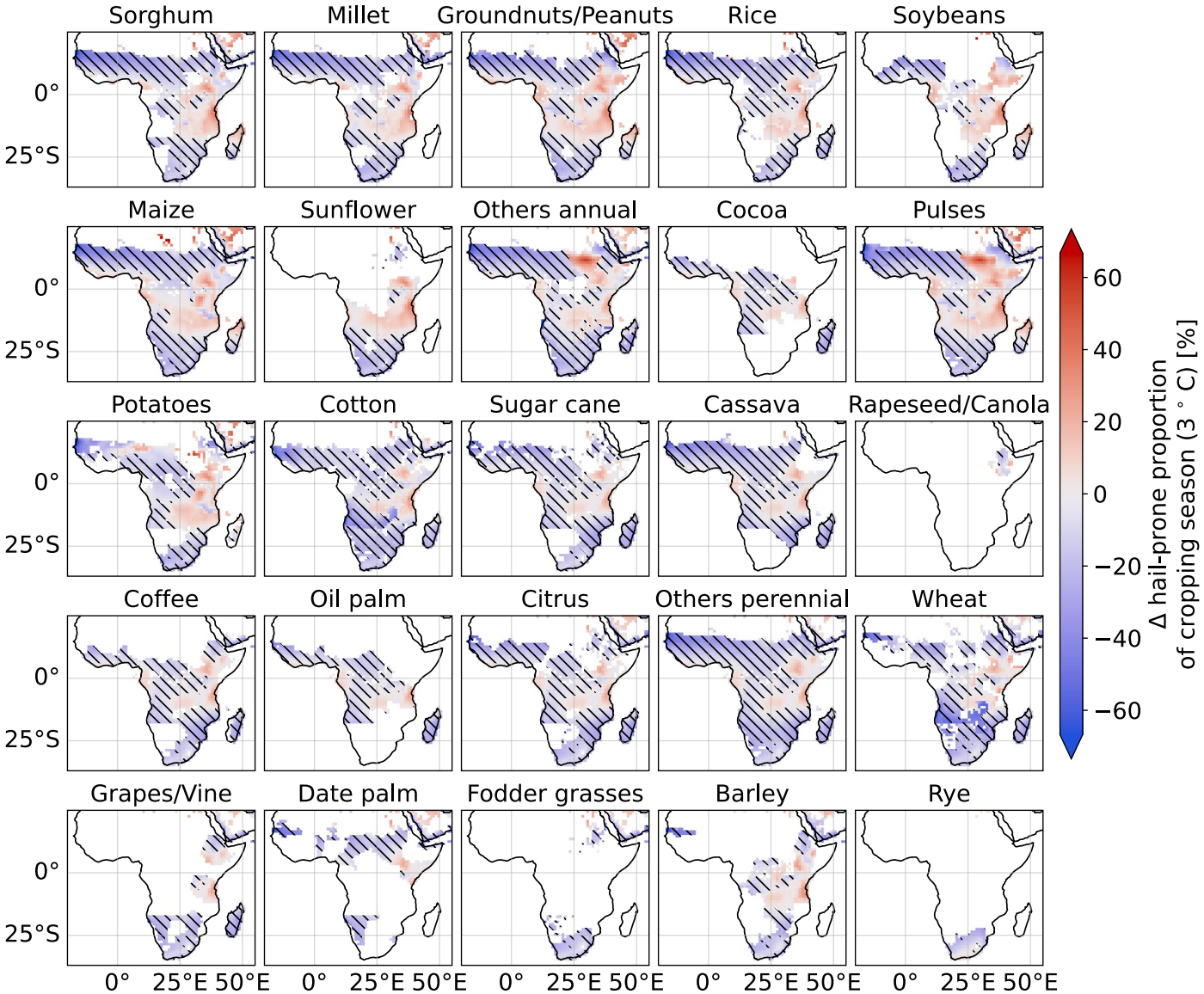

Extended Data Fig. 4 | Regional, relative changes in hail-prone proportion of cropping season for Africa. Change in multimodel, multi-proxy mean hail-prone proportions (n = 480) of cropping seasons for 3 °C warming, for Africa, with changes shown as percentages of the mean historical hail-prone proportion (n = 480) of cropping season. Crops for which there were no significant changes recorded are not shown. Stippling shows regions in which at least 50% of the model/proxy combinations agreed with the sign of the mean difference and also showed significant differences in the mean ($p < 0.05$ on a two-sided Welch's t-test, n = 20 years per epoch). The colour bar is truncated to the range of stippled values.

https://doi.org/10.1038/s41558-026-02660-7

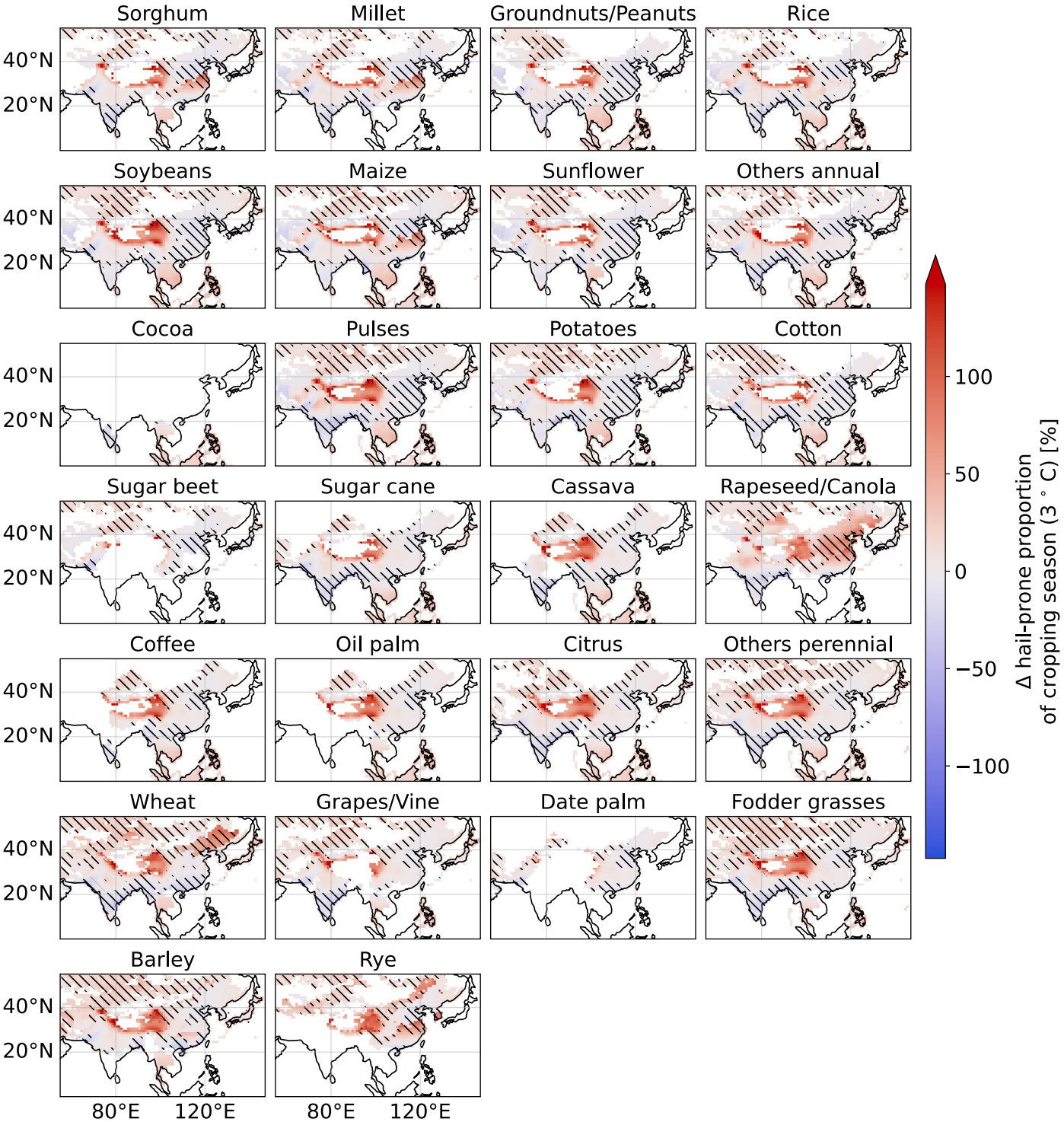

Extended Data Fig. 5 | Regional, relative changes in hail-prone proportion of cropping season for Asia. As for Extended Data Fig. 4 but for Southern, Eastern, Northern, and northern South-eastern Asia.

https://doi.org/10.1038/s41558-026-02660-7

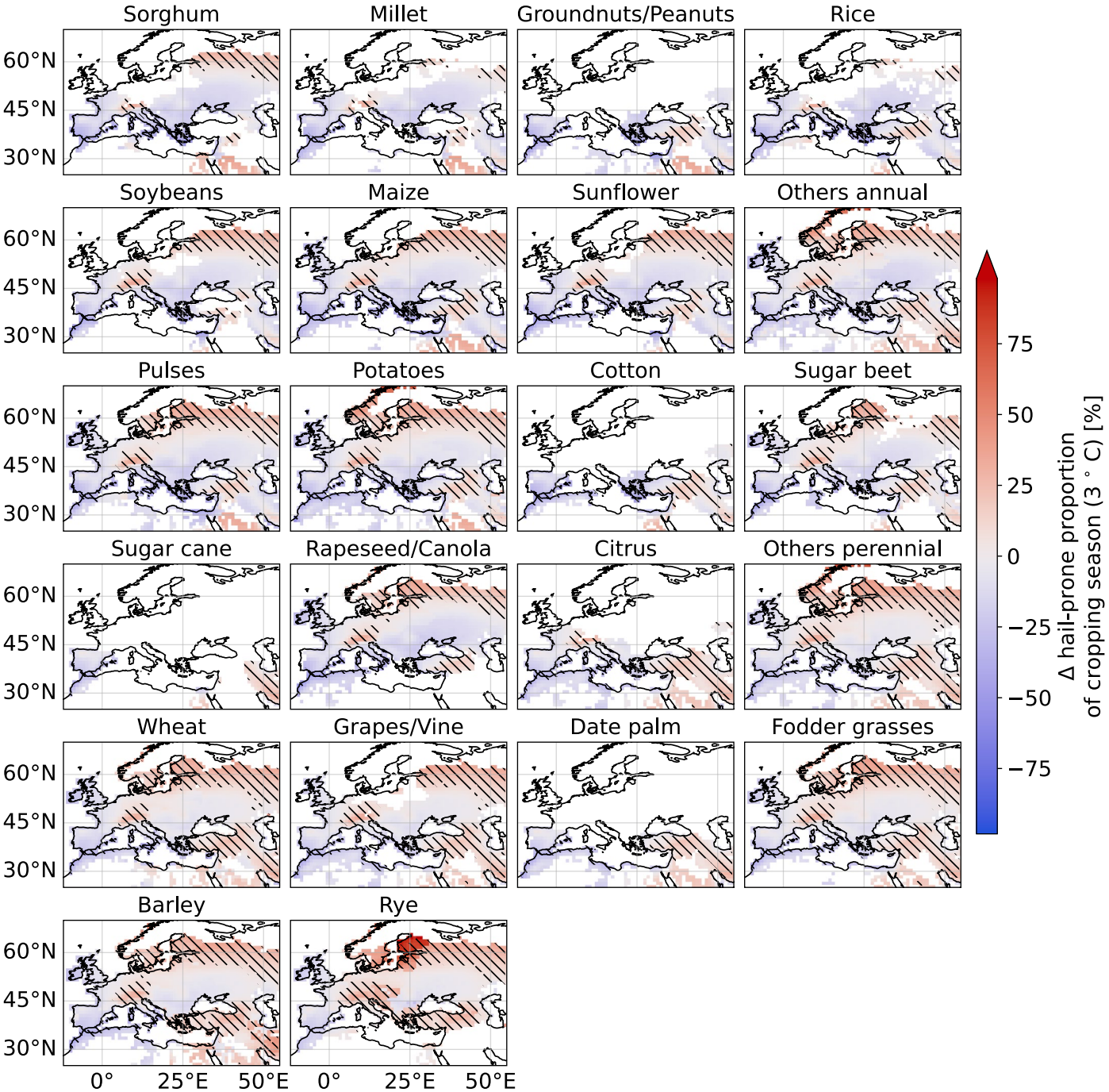

Extended Data Fig. 6 | Regional, relative changes in hail-prone proportion of cropping season for Europe. As for Extended Data Fig. 4 but for Europe, Northern Africa, Western Asia, and Iran.

https://doi.org/10.1038/s41558-026-02660-7

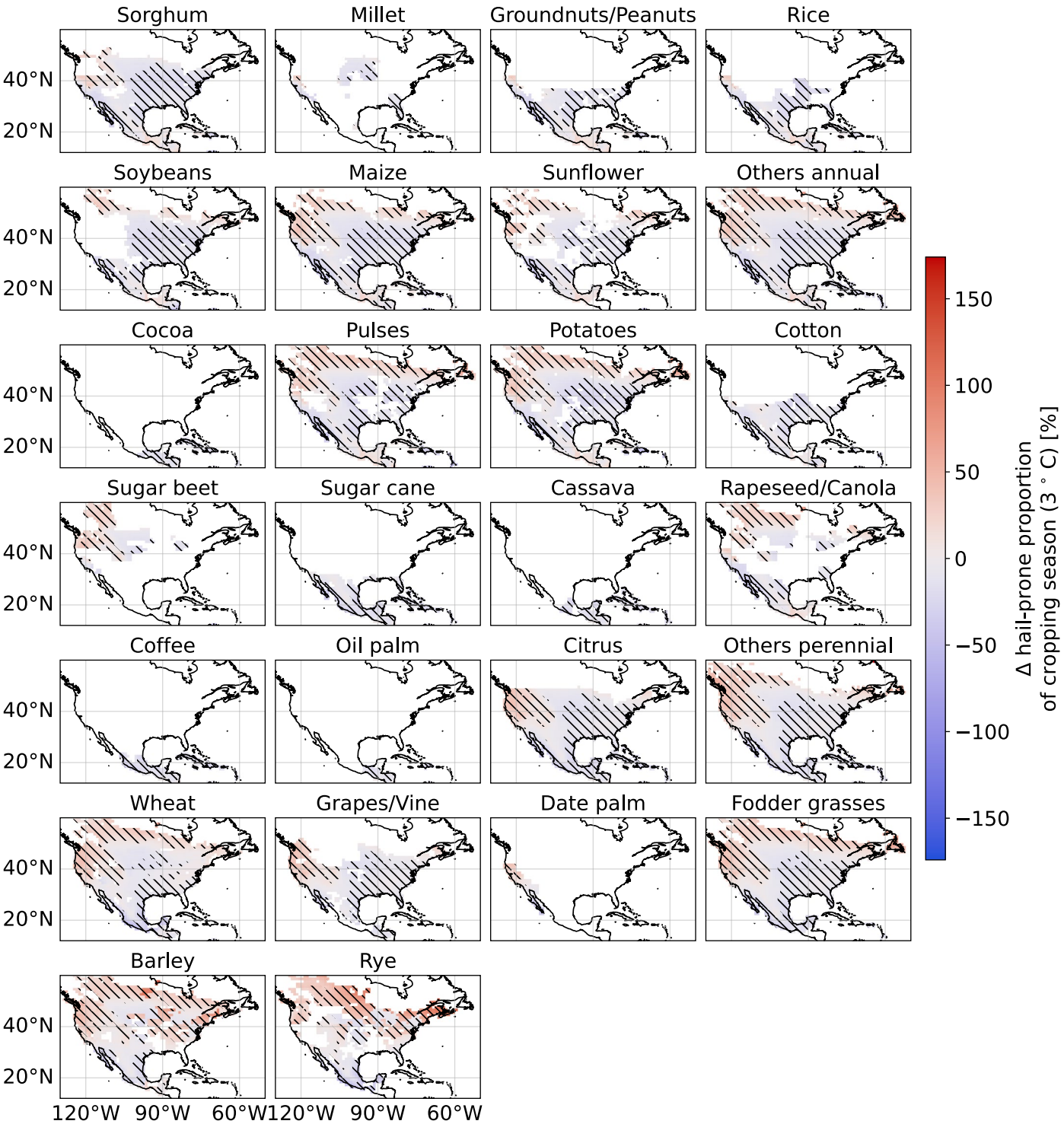

Extended Data Fig. 7 | Regional, relative changes in hail-prone proportion of cropping season for Northern America. As for Extended Data Fig. 4 but for Northern America, Central America, and the Caribbean.

https://doi.org/10.1038/s41558-026-02660-7

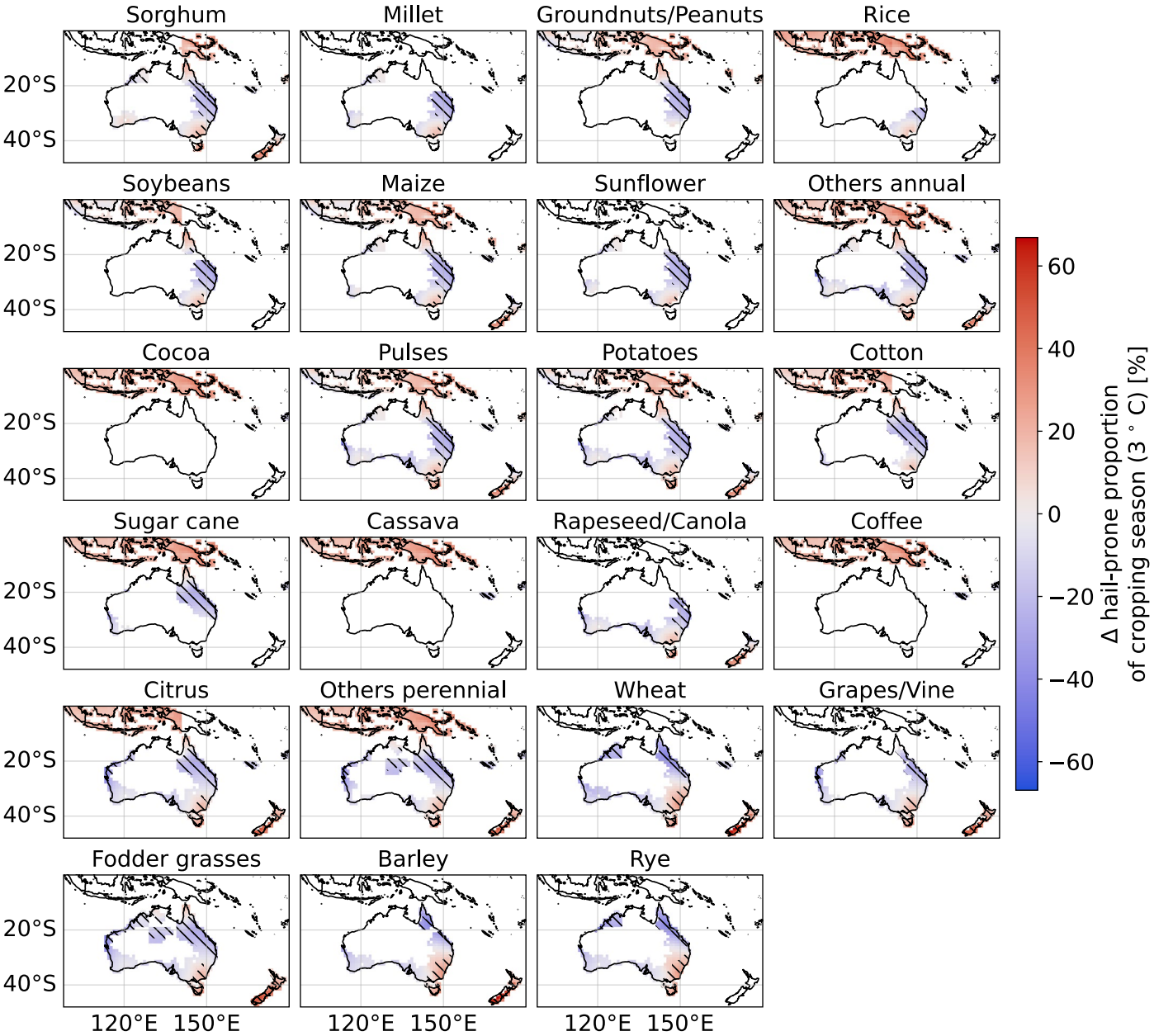

Extended Data Fig. 8 | Regional, relative changes in hail-prone proportion of cropping season for Oceania. As for Extended Data Fig. 4 but for Oceania and southern South-eastern Asia.

https://doi.org/10.1038/s41558-026-02660-7

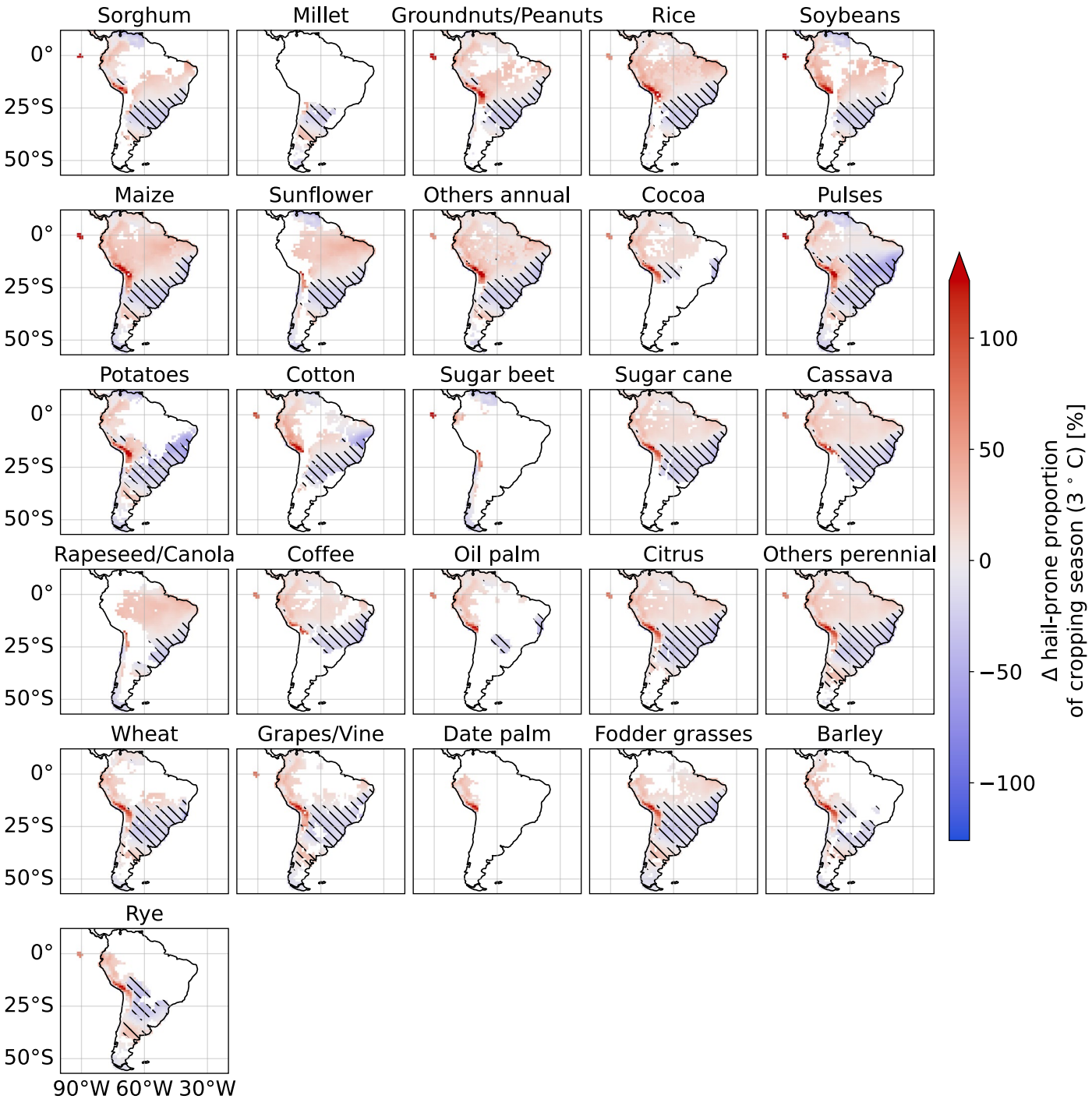

Extended Data Fig. 9 | Regional, relative changes in hail-prone proportion of cropping season for South America. As for Extended Data Fig. 4 but for South America.

https://doi.org/10.1038/s41558-026-02660-7

Extended Data Table 1 | Numbers of samples in box plots

Region	Africa		Asia		Europe		Global		N. America		Oceania		S. America	
Epoch	2°C	3°C	2°C	3°C	2°C	3°C	2°C	3°C	2°C	3°C	2°C	3°C	2°C	3°C
Crop														
Barley	329	341	725	1024	487	732	2735	3601	675	853	87	144	193	263
Cassava	1115	1064	463	601			2217	2256	154	157	18	20	460	404
Citrus	974	984	652	896	167	310	3165	3843	631	843	211	245	508	514
Cocoa	576	524	60	51			903	816	115	113	6	8	146	120
Coffee	774	763	410	522			1735	1800	161	165	18	20	360	318
Cotton	881	1074	731	892	127	210	2490	2960	315	341	122	136	312	304
Date palm	425	445	222	319	124	219	796	1037	16	40			8	7
Fodder grasses	121	167	1059	1337	511	727	3619	4516	887	1112	276	318	500	562
Grapes/Vine	293	340	713	942	373	569	2639	3394	433	614	146	177	422	485
G.nuts/Peanuts	764	862	645	727	82	152	2145	2454	275	307	73	91	306	310
Maize	860	976	776	998	307	501	3347	4189	709	926	119	147	320	375
Millet	792	901	647	838	61	171	1876	2437	55	92	74	94	92	157
Oil palm	606	558	296	415			1066	1129	57	56			107	100
Others annual	1050	1107	832	1054	383	652	3933	4837	875	1112	138	176	386	414
Others perennial	1317	1333	984	1258	544	776	4762	5652	846	1078	251	291	527	572
Potatoes	480	568	927	1092	429	662	3313	4172	821	1014	120	165	285	401
Pulses	745	851	938	1148	376	565	3616	4459	738	900	124	166	427	543
Rapeseed/Canola	16	22	463	809	314	507	1654	2318	365	436	66	102	210	192
Rice	930	971	555	645	123	254	2325	2638	294	324	18	36	348	344
Rye	3	21	401	638	396	600	1713	2582	453	684	95	152	125	242
Sorghum	819	946	626	819	191	322	2771	3502	499	666	132	172	285	328
Soybeans	389	442	848	959	258	396	2531	3032	487	625	62	85	239	267
Sugar beet			505	601	263	446	1001	1359	155	218			3	8
Sugar cane	981	969	514	666	58	103	2415	2588	259	276	115	122	479	431
Sunflower	222	311	757	877	280	428	2337	2925	467	644	91	110	277	302
Wheat	698	810	796	1220	470	670	3327	4399	609	802	132	196	383	457

Numbers of samples (grid points with significant changes) used to generate each box plot in Fig. 6. 'N. America' stands for North America, 'S. America' for South America, and 'G.nuts' for groundnuts.